Mixed-Layer Budget Analysis of the Diurnal Cycle of Entrainment in SE Pacific Stratocumulus

PETER CALDWELL* , CHRISTOPHER S. BRETHERTON, and ROBERT WOOD

University of Washington, Seattle, Washington

October 22, 2004

Corresponding author address: Peter Caldwell, University of Washington, Department of Atmospheric Sciences, Box 351640, Seattle, WA 98195-1640. E-mail: caldwep@atmos.washington.edu.

Abstract

Mixed-layer budgets of boundary layer mass, moisture, and liquid water static energy are estimated from six days of data collected at 85°W, 20°S (a region of persistent stratocumulus) during the East Pacific Investigation of Climate stratocumulus cruise in 2001. These budgets are used to estimate a mean diurnal cycle of entrainment and, by diagnosing the fluxes of humidity and liquid water static energy necessary to maintain a mixed-layer structure, of buoyancy flux. Although the entrainment rates suggested by each of the budgets have significant uncertainty, the various methods are consistent in predicting a 6-day mean entrainment rate of 4 ± 1 mm s^{-1}, with higher values at night and very little entrainment around local noon. The diurnal cycle of buoyancy flux suggests that drizzle, while only a small term in the boundary-layer moisture budget, significantly reduces sub-cloud buoyancy flux and may induce weak decoupling of surface and cloud-layer turbulence during the early morning hours, a structure which is maintained throughout the day by shortwave warming. Finally, the diurnal cycle of entrainment diagnosed from three recently-proposed entrainment closures is found to be consistent with the observationally-derived values.

1 Introduction

Marine boundary layer (BL) clouds blanket more than a quarter of the globe and are associated with a strongly negative cloud radiative forcing (Hartmann et al., 1992), felt both in the atmosphere and in the ocean. Because of this, their realistic simulation is important for modern climate modeling. The horizontal and vertical grid resolution in current climate models, however, is much too coarse to resolve the fine-scale processes governing these clouds, so the task is left to parameterization. Unfortunately, the interaction between stratus clouds and their environment is complex and poorly understood. As a result, current general circulation models have difficulty reproducing the current mean low cloud amount (Weare, 1996) and diurnal cycle (Duynkerke and Teixeira, 2001).

In the subtropics, stratocumulus-capped BLs stretch across vast regions to the west of the subtropical continents, where cool, equator-moving ocean currents meet warm, subsiding air from the Hadley circulation. The 2001 East Pacific Investigation of Climate (EPIC) stratocumulus study was designed to improve our understanding of these clouds and thus aid in their parameterization (Bretherton et al., 2004). The southeast (SE) Pacific stratocumulus region, site of the EPIC cruise, is one of the largest and most persistent area of subtropical stratus in the world (Klein and Hartmann, 1993), but has received much less attention than similar areas in the northern hemisphere. If cloud dynamics and microphysics were similar in all regions, this neglect would not be noteworthy. Cloud condensation nuclei, however, are probably scarcer in SE Pacific stratocumulus than in similar clouds in the northeast Pacific, with as-yet uncertain mi-

crophysical impacts. Additionally, the SE Pacific stratocumulus region has an unusually large and regular diurnal cycle (Rozendaal et al., 1995; Wood et al., 2002), which has a strong effect on the BL and surface energy balance since clouds only reflect and absorb sunlight during daylight hours. In addition, diurnal variation is an excellent test of climate models since it is an observable and reproducible response to radiative forcing (Randall et al., 2003).

A study of diurnal variation is well-suited to the EPIC data, which documents a strong diurnal cycle with three-hourly radiosonde observations and extensive remote sensing from aboard the NOAA ship Ronald H. Brown (RHB). In particular, we will use A 6-day 'buoy-period' (Oct 16th-22nd, 2001), during which the ship was stationed at a Woods Hole Oceanographic Institute (WHOI) buoy at 20°S, 85°W for our analysis. Bretherton et al. (2004) summarizes the observations and initial findings from this period. Radiosondes, launched from the RHB every 3 hours from 2 UTC on the 16th to 23 UTC on the 21st, reveal little BL stratification, with vertical gradients in liquid static energy (s_l) generally less than 2 kJ kg^{-1} and gradients in total water mixing ratio (q_t) of less than 1.5 g kg^{-1} over the BL depth of 1.2-1.4 km. Assuming the BL to be completely well mixed allows us to infer certain aspects of the diurnal cycle of turbulence. Analysis neglecting stratifying effects is commonly called the mixed-layer approximation and has a long history in the literature (Lilly, 1968; Schubert et al., 1979; Bretherton and Wyant, 1997). Under this approximation, turbulent mixing is assumed to dominate stratification so that thermodynamic properties closely follow adiabatic profiles (Albrecht et al., 1990;

Wood and Taylor, 2001). While previous studies have used this simplification primarily in modeling and theoretical work, we follow Nicholls (1984) in employing the mixed-layer assumption as a simplifying framework for deriving BL turbulent flux profiles from a limited set of observations.

This structure is helpful, because although satellite and shipboard measurements have been useful for diagnosing the diurnal cycle of some radiatively important properties of stratocumulus clouds such as cloud fraction and liquid water path (LWP), other properties such as drizzle and turbulence are more difficult to detect and as such have only been documented by a limited number of in-situ studies, mostly in near-coastal regions affected by sea-breezes (Brost et al., 1982; de Roode and Duynkerke, 1997; Hignett, 1991; Nicholls and Leighton, 1986). Because stratocumulus clouds owe their existence to an intricate web of feedbacks involving surface fluxes, turbulence, large-scale subsidence, radiation, and cloud microphysics, better assessment of these difficult-to-measure quantities is essential. In a mixed layer context, these feedbacks interact to regulate the entrainment rate - the rate of BL growth due to the incorporation of free-tropospheric air by turbulence. By controlling the growth rate of the BL and its intake of warm, dry air from the free troposphere, entrainment plays a key role in determining climatologically important parameters such as liquid water path (LWP) and BL depth. Despite over 35 years of investigation, though, there is still controversy over how this process should be parameterized. Recent entrainment schemes vary by as much as a factor of two in their predictions of steady-state cloud-top height and LWP (Stevens, 2002), emphasizing the

need for additional observational evidence to better constraint entrainment. Thus the main focus of this paper is to use observations taken during the EPIC cruise to provide estimates of the diurnal cycle of entrainment in the SE Pacific stratocumulus region and to assess its sensitivity to drizzle, LWP, and the inferred intensity of BL turbulence.

The remainder of the paper is divided into four sections. A derivation of the budget and flux equations used in this study is presented in section 2. The relevant data are explained in section 3. Section 4 covers the results and is followed by conclusions in section 5.

2 Methodology

2.1 Budget Equations and Entrainment Rates

We have computed budgets of BL mass, heat, and moisture. The thermodynamic budgets are based on variables approximately conserved under adiabatic displacements and phase changes. The first, total water mixing ratio $q_t = q_v + q_l$, is the sum of the water vapor mixing ratio q_v and (where the air is saturated) the cloud liquid water mixing ratio q_l. The second is the liquid static energy, $s_l = c_p T + gz - Lq_l$, where T and z are temperature and height and c_p, L, and g are (respectively) the isobaric heat capacity of dry air, the latent heat of water vaporization, and the gravitational acceleration. Although c_p varies slightly with q_t and L varies slightly with T, the variations are minor, so constant values of 1004 J kg^{-1} K^{-1} and 2.5×10^6 J kg^{-1} are assumed in this study. Because the BL during EPIC was fairly deep, a vertical 'pressure-height' coordinate $\hat{p} = p_0 - p$, equal

to the difference between the instantaneous surface pressure p_0 and the actual pressure p, was adopted to avoid the small but quantitatively significant errors associated with a constant-density assumption. Under this framework, we arrive at horizontally- and BL-averaged budget equations for q_t and s_l (derived in the appendix)

$$\hat{p}_i \left[\frac{\partial \langle q_t \rangle}{\partial t} + \langle \mathbf{v} \cdot \nabla_h q_t \rangle \right] - g \frac{\mathrm{LHF}}{L} - g F_P(0) - \hat{\omega}_e \Delta q_t = \left[\langle q_t \rangle - q_{t-} \right] \mathbf{v} \cdot \nabla_h \hat{p}_i \qquad (1)$$

$$\hat{p}_i \left[\frac{\partial \langle s_l \rangle}{\partial t} + \langle \mathbf{v} \cdot \nabla_h s_l \rangle \right] - g\,\mathrm{SHF} + gL \cdot F_P(0) + g\,\nabla_{\mathrm{BL}} F_R - \hat{\omega}_e \Delta s_l = -\left[\langle s_l \rangle - s_{l-} \right] \mathbf{v} \cdot \nabla_h \hat{p}_i \qquad (2)$$

where the operator $\langle x \rangle$ denotes the mass-weighted BL average of a given quantity x, $\mathbf{v} \cdot \nabla_h x$ represents the horizontal advection of x into our layer of interest, Δx is the difference between the value of x just above the BL-capping inversion and $\langle x \rangle$, and x_- is the value of x just below the inversion. In addition, $F_P(\hat{p})$ (negative because it is a downward water flux) is the horizontally-averaged precipitation rate at pressure-height $\hat{p}$ and $\nabla_{\mathrm{BL}} F_R = F_R(\hat{p}_i) - F_R(0)$ is the divergence of net radiative flux between the BL top, $\hat{p}_i$, and the surface. The entrainment rate, w_e, is expressed here in $\hat{p}$-coordinates as $\hat{\omega}_e = \rho g \cdot w_e$.

In an idealized mixed layer, the conserved quantities are equal to their BL-averaged value below cloud top, so mixed-layer analyses typically neglect the terms on the right-hand side of (1) and (2). In the present study, we have estimated the effect of these terms to always be less than 2 W m^{-2}, which is small compared to the other budget terms and to the measurement uncertainty (see Tables 1 and 2). For this reason, the rest of this paper focuses on the mixed-layer version of these equations. A cartoon showing

the fluxes which contribute to each mixed-layer budget is included in Fig. 1.

Using observationally-derived estimates of the surface and precipitation fluxes and inferring radiative fluxes from thermodynamic and liquid water profiles, we can estimate all terms in (1) and (2) except the entrainment fluxes. Thus estimates of $\hat{\omega}_e$ may be derived as budget residuals of (1) and (2). A third independent estimate of $\hat{\omega}_e$ may be obtained from the BL mass budget. BL mass (given by $\hat{p}_i/g$ in the current coordinate system) changes as a result of imbalance between mass influx due to entrainment and mass outflux caused by subsidence, $\hat{\omega}_s = \partial \hat{p}_i/\partial t$. In equation form this reduces to

$$\frac{\partial \hat{p}_i}{\partial t} + \mathbf{v} \cdot \nabla_h \hat{p}_i = \hat{\omega}_e + \hat{\omega}_s. \tag{3}$$

By using radar data, satellite measurements, and large-scale gridded analyses to estimate $\partial \hat{p}_i/\partial t$, $\mathbf{v}\cdot\nabla_h \hat{p}_i$, and $\hat{\omega}_s$, respectively, $\hat{\omega}_e$ may also be diagnosed from (3). The consistency of the entrainment rates inferred from each of the three budgets is an important check on the plausibility of our results.

2.2 Turbulent Flux Profiles

2.2.1 Conserved-Variable Fluxes

The tendencies of total water mixing ratio and liquid water static energy satisfy

$$\frac{\partial q_t}{\partial t} = -\frac{\partial W}{\partial \hat{p}} \tag{4}$$

and

$$\frac{\partial s_l}{\partial t} = -\frac{\partial E}{\partial \hat{p}}, \tag{5}$$

where

$$W(\hat{p}) = \overline{\hat{\omega}' q_t'} + g\, F_P(\hat{p}) \tag{6}$$

and

$$E(\hat{p}) = \overline{\hat{\omega}' s_l'} + g\,[F_R(\hat{p}) - L \cdot F_P(\hat{p})] \tag{7}$$

are total fluxes of water and liquid static energy, respectively. In these equations, positive flux indicates upward transport. The overbar is used here to emphasize the horizontal averaging process, while primes denote perturbations from this average.

For the BL to remain well mixed, q_t and s_l tendencies must be uniform with height. Thus $W(\hat{p})$ and $E(\hat{p})$ must be linear functions of $\hat{p}$, uniquely determined by their surface and cloud-top values,

$$W(0) = g\,[\mathrm{LHF}/L + F_P(0)]\,, \tag{8}$$

$$E(0) = g\,[\mathrm{SHF} - LF_P(0) + F_R(0)]\,, \tag{9}$$

$$W(\hat{p}_i) = -\hat{\omega}_e \Delta q_t, \tag{10}$$

and

$$E(\hat{p}_i) = -\hat{\omega}_e \Delta s_l + g\, F_R(\hat{p}_i). \tag{11}$$

By expressing $W(\hat{p})$, $E(\hat{p})$ in terms of their surface and cloud-top values and solving (6) and (7) for the corresponding turbulent fluxes, equations for the turbulent flux profiles of q_t and s_l may be obtained.

2.2.2 Buoyancy Fluxes and Convective Velocity

For a typical subtropical stratocumulus-capped BL, the main source of turbulent kinetic energy is buoyancy flux

$$\mathcal{B} = \frac{1}{\rho\, s_{v0}} \overline{\hat{\omega}' s_v'}. \tag{12}$$

Here, the virtual static energy $s_v = c_p T_v + gz$ is defined in terms of virtual or 'density' temperature (including liquid loading) $T_v = T + T_{\rm ref}(\delta q_v - q_l)$, where $\delta = 0.608$ and $T_{\rm ref} = 290$K. The term s_{v0} is a reference virtual static energy (computed here at a reference pressure height of 5mb).

We now relate $\mathcal{B}$ to the conserved variable fluxes following Bretherton and Wyant (1997) but working in terms of liquid static energy rather than moist static energy. Using the definition $s_l = c_p T + gz - L q_l$, s_v may be rewritten as

$$s_v = s_l + (1-\epsilon) L q_l + \delta \epsilon L q_v \tag{13}$$

where $\epsilon = c_p T_{\rm ref}/L \approx 0.1$. Expressing this quantity in terms of the conserved variables is particularly simple below cloud base, as $q_l = 0$ and thus $q_v = q_t$. Within the cloud, q_v is assumed equal to the saturation mixing ratio, $q_{\rm sat}$, so that

$$\begin{aligned} q_v' &= \frac{\partial q_{\rm sat}}{\partial T} T' \\ &= \frac{1}{c_p} \frac{\partial q_{\rm sat}}{\partial T} \left[s_l' - L \cdot (q_t' - q_v') \right]. \end{aligned}$$

Solving this last equation for q_v' and setting $\gamma = L/c_p \cdot \partial q_{\rm sat}/\partial T$, we can express (13) in terms of s_l' and q_t' in the cloud layer. Together, the sub-cloud and in-cloud forms of (13)

imply

$$\overline{\hat{\omega}' s_v'} = \begin{cases} \overline{\hat{\omega}' s_l'} + \delta\epsilon L \overline{\hat{\omega}' q_t'}, & 0 < \hat{p} < \hat{p}_{cb} \\ \beta \overline{\hat{\omega}' s_l'} + (\beta - \epsilon) L \overline{\hat{\omega}' q_t'}, & \hat{p}_{cb} < \hat{p} < \hat{p}_i. \end{cases} \tag{14}$$

Here, $\hat{p}_{cb}$ is the cloud-base pressure-height and $\beta = [1 + \epsilon\gamma(\delta + 1)] / (\gamma + 1) \approx 0.5$ is a weak function of pressure and temperature (Randall, 1980).

The convective velocity scale, w_*, a measure of the overturning velocity of buoyantly driven eddies, is then calculated as

$$w_* = \left[2.5 \frac{z_i}{\hat{p}_i} \int_0^{\hat{p}_i} \mathcal{B} d\hat{p} \right]^{\frac{1}{3}} \tag{15}$$

where z_i is the BL depth expressed in meters. Here, we have adapted the standard definition of w_* (e.g. Nicholls and Turton (1986)) to $\hat{p}$ coordinates based on the derivation of a turbulent kinetic energy equation from the same governing equations in $\hat{p}$ coordinates used to derive (1) and (2).

3 Data

3.1 Mass Budget

We assume (consistent with soundings) that cloud-top always coincides with inversion base. Thus entrainment may be calculated from (3) by combining measurements of cloud-top height tendency, subsidence rate, and advection of cloud-top height. During the cruise, measurements of cloud-top height were obtained at 15 second resolution from a vertically pointing 35 GHz cloud radar. This data was averaged into 3-hour means with the first mean centered at 2 UTC on the 16th; $\partial \hat{p}_i / \partial t$ was then approximated using cen-

tered differencing. Estimates of subsidence rate at the buoy location were obtained from 12-35 hour forecasts (obtained at full model vertical resolution) by both the European Center for Medium Range Weather Forecasting (ECMWF) operational forecast model (courtesy of Martin Köhler at ECMWF) and the National Center for Environmental Prediction (NCEP) medium-range forecast model (courtesy of Hua-Lu Pan at NCEP and Steve Krueger at the University of Utah). These models assimilated surface meteorological data from the WHOI buoy but not from the RHB radiosonde soundings described in the next section. Advection of inversion height is assumed to have a constant value of 0.49 mm s^{-1}, diagnosed as the large-scale slope of satellite-derived cloud-top height based on a climatology from Oct-Nov 2000 - a comparable season (Wood and Bretherton, 2004). We chose this estimate despite probable synoptic and diurnal variations in the advection of inversion height, noting that because its climatological mean value is small, exact diagnosis of cloud-top height advection is probably not important to the analysis of the mass budget.

3.2 Moisture and Liquid Static Energy Budgets

For our budgets, we compute BL-averaged q_t and s_l from the radiosonde profiles at each launch time as the mean of the profile over the layer from 50m above the surface to the base of the inversion capping the BL. The 50m lower limit was chosen to avoid errors associated with ship-deck heating. The inversion base was chosen by eye as the height at which q_t begins to drop from relatively large BL values (typically 8 g kg^{-1}) to the

extremely dry values found in the overlying air (usually 2 g kg^{-1} or less). The q_t and s_l profiles are computed by combining radiosonde-derived measurements of q_v and T with estimates of q_l. A q_l profile was estimated for each 3 hour period by assuming liquid water content increases linearly from a cloud base value of zero to a cloud-top value such that $1/g \int_{\hat{p}_b}^{\hat{p}_t} q_l d\hat{p}$ matches the observed liquid water path. Liquid water path was obtained at 5 min resolution from a NOAA shipboard microwave radiometer following Hogg et al. (1983). This quantity, and all others obtained at higher-than-radiosonde resolution, was averaged into 3 hour means centered on the radiosonde launch times. One exception, however, is cloud base, which was obtained at 15 second resolution from NOAA Environmental Technology Laboratory (ETL) ceilometer. The lowest altitude return was composited into hourly median values before averaging into 3 hour means about the radiosonde launch times. This added complexity was introduced to avoid bias introduced by large outliers in the apparent cloud base that we believe was a ceilometer response to intermittent sub-cloud drizzle. Three-hour average cloud fraction was also inferred from the ceilometer. Density is derived from the ideal gas law. Time derivatives of $\langle q_t \rangle$ and $\langle s_l \rangle$ are computed using centered differencing. Advective terms are estimated from the ECMWF and NCEP forecasts mentioned in section 3.1. Results from both models are compared in subsection 4.

Surface sensible and latent heat fluxes are derived from temperature and humidity measurements taken on the RHB instrumented tower (14 m altitude) using the bulk flux algorithm described by Fairall et al. (1996), who estimated the error in these fluxes to be

less than 5 W m^{-2}. The fluxes agreed to within this accuracy with similarly-derived fluxes from buoy measurements when the ship and buoy were collocated. Cloud base precipitation averaged over a 30 km radius centered on the ship was diagnosed from C-band radar, then expanded into precipitation flux profiles by a sedimentation/evaporation model based on theoretical reflectivity profiles generated using ETL's millimeter-wavelength vertically pointing radar on the RHB as described in detail by Comstock et al. (2004). Radiative fluxes are computed by BUGSRAD, a two-stream correlated-K radiative transfer scheme developed at Colorado State University (Stephens et al., 2001). Both satellite and cloud radar observations did not detect any cloud above the BL over the RHB during the six-day period. In order to obtain realistic fluxes for partly cloudy conditions, results from clear and cloudy sky radiative-transfer calculations were combined in an average which was weighted by the ceilometer-derived cloud fraction. The cloudy-sky calculation was based on the 3-hour average liquid water profile rescaled by dividing by the cloud fraction. To overcome the lack of radiosonde data at higher altitudes, missing profile data below 15km were interpolated from neighboring profiles, and above 15km all profiles were blended into the McClatchey et al. (1971) standard tropical atmospheric profiles. As discussed by Bretherton et al. (2004), cloud droplet number concentrations were estimated during daylight hours from simultaneous measurements of cloud thickness, LWP, and cloud optical depth following Dong and Mace (2003). Nighttime values were then generated by linear interpolation. Comparison between calculated and observed downwelling radiative fluxes at the surface (Fig. 2) shows our approach to

slightly underestimate surface shortwave fluxes, although comparison with simultaneous observations from the WHOI buoy (included as triangular and circular points) suggests that this discrepancy lies within the realm of sampling uncertainty. Triangular markers denote times when the ship and buoy were collocated, so serve as a strict measure of instrument calibration uncertainty. Circular markers indicate times when the ship was away from the buoy (typically by less than 20km) and thus show the effect of mesoscale variability on radiative fluxes. Since our radiative profiles are derived from a single sounding while the shipboard radiometer data is averaged over 3 hrs, it is unsurprising that the disagreement between the derived fluxes and the shipboard observations is of similar magnitude to that shown by the circular markers. Although the differences between ship observations and radiative transfer calculations are sometimes quite large, it is important to remember that it is only the atmospheric radiative heating driven by clouds that enters our calculations. Because clouds absorb only a small fraction of the impinging solar radiation, errors in the BL net shortwave flux divergence can be expected to be much less than errors in the surface downwelling solar radiation. Calculated longwave fluxes agree quite well with the observations, with perhaps a 5 W m^{-2} high bias for lower fluxes (eg decreased cloudiness).

3.3 Cross-Inversion Jumps

A practical complication of imposing a mixed layer idealization on any real BL is how to optimally determine inversion jumps. A particular issue during EPIC was apparent

systematic errors in radiosonde-derived temperature profiles just above the inversion. Fig. 3 compares the q_v and T soundings from a typical radiosonde launch, 2 UTC on Oct 16. In this figure, the inversion thickness diagnosed from the q_v sounding is around 3mb ($\sim$30m) - a value consistent with the literature (Caughey et al., 1982; Lenschow et al., 2000). The T sounding, however, has a 15mb ($\sim$150m) layer where T increases with height, rather than a jump-like inversion. The reason for this discrepancy is still unclear. Clear-air radiative cooling above the inversion top and temperature sensor response lags were considered, but cannot explain the nearly linear increase in temperature over such a deep layer. One possibility is that cloud droplets wet the sensor as it passes through cloud, and subsequently interfere with sensor response above cloud through evaporative cooling. Comparison of radiosonde and simultaneous aircraft/dropsonde measurements or laboratory experiments on the effect of wetting on radiosonde temperature sensors would be useful for investigating the cause of this problem.

To avoid using temperature measurements in this uncertain region to compute cross-inversion jumps, we infer s_l at the top of the entrainment layer from its value some distance above. In order to account for the radiative cooling taking place as air subsides from the height where it is measured to the height at which it is entrained, a correction offset is applied. Ideally, this offset would depend on the time-varying entrainment rate and the above-inversion moisture profile, among other quantities difficult to assess from the available data. After discovering that more sophisticated approaches all occasionally predicted unreasonably large corrections due to this uncertainty, we applied a single

correction to all soundings. This correction is derived by considering the evolution of s_l in the layer above the inversion, which may be written in a cloud-top-relative coordinate system (with vertical coordinate $\zeta = \hat{p} - \hat{p}_i$) as

$$\frac{\partial s_l}{\partial t} + \mathbf{v} \cdot \nabla_h s_l - \hat{\omega}_e \frac{\partial s_l}{\partial \zeta} = -g \frac{\partial F_R}{\partial \zeta}. \tag{16}$$

The horizontal gradient is taken here along a surface of constant ζ. Averaged over the 6 day period, the soundings imply that $\partial s_l / \partial t$ is negligible. Thus (16) reduces to a balance between horizontal advection, subsidence warming and radiative cooling. Corrections to the 6-day mean s_l profile just above the cloud top were made by forcing the s_l profile in the lowest 30mb above the inversion to obey this balance by running (16) to equilibrium using upstream differencing to resolve the sharp gradient at cloud top. In this calculation, radiative fluxes were derived using the BUGSRAD scheme. The 6-day mean $\hat{\omega}_e$ =3.5 mm s^{-1} is estimated in sec. 4.1 using the mass budget (3) with ECMWF subsidence, which we show in 4.2.2 to also be consistent with the 6-day mean BL s_l and q_t budgets. The vertical profile of advection may be diagnosed in the region overlying the layer we hope to correct as the residual of (16) with $\partial s_l / \partial t = 0$. This residual, presented in Fig. 4a as the difference between subsidence warming and radiative cooling, appears to decrease linearly with height above about $\hat{p}_i$+30mb. Based on this observation, we approximate horizontal advection by a linear least-squares fit to the subsidence warming/radiative cooling residual in the region topping the inversion by 30 to 75 mb. This process results in a horizontal advection tendency given by

$$\mathbf{v} \cdot \nabla_h s_l = 8.5 \times 10^{-2} - 3.78 \times 10^{-4} \cdot \hat{p}. \tag{17}$$

Just above the inversion, this method suggests an s_l advection of 2.8 kJ kg^{-1} day^{-1}. Because this measure of advection ceases to match the predictions of Fig. 4a below $\hat{p}_i$+30mb, we choose our correction layer to extend from the inversion base to this level. The depth of this layer also happens to be the distance a typical air parcel will subside in a day, so correcting over this depth has the added advantage that it facilitates using an entrainment rate which has been averaged over the diurnal cycle and is therefore more robust.

Fig. 4b shows the results of the correction process. Comparison of the original and corrected s_l profiles serves as a further illustration of how out of balance the uncorrected profiles were. The shaded region on this graphic depicts the engulfment layer - the layer from which air is typically entrained. The depth of this layer is a rather uncertain quantity; we take the engulfment layer depth to be 8 mb based on recent analysis from aircraft flights in the Californian stratus region by Faloona et al. (2004) and estimate the liquid static energy of entrained air to be the mean value of the corrected s_l profile over this layer. Application of this definition to Fig. 4b implies that s_l at $\hat{p}_i$ should be reduced by a correction $s_{l,\mathrm{corr}}$ of 4.0 kJ kg^{-1} in order to properly represent the value entrained. In the absence of a reliable time-varying correction, we diagnose the value of s_l entrained at each time by subtracting 4.0 kJ kg^{-1} from the value of s_l calculated from the sounding at 30mb above $\hat{p}_i$.

In an effort to avoid problems associated with variations in inversion depth, above-inversion total water mixing ratio is sampled at 10mb above the BL. Because q_t is

approximately constant in the free troposphere, this value is used in Δq_t without adjustment.

4 Results

4.1 Entrainment from the Mass Budget

Fig. 5 presents the diurnal cycles of $\hat{\omega}_s$, $\partial \hat{p}_i / \partial t$, and $\hat{\omega}_e$ (calculated as a budget residual of (3) using $\hat{\omega}_s$, $\partial \hat{p}_i / \partial t$, and the assumed horizontal advective inversion-height tendency). Both ECMWF and NCEP analyses of $\hat{\omega}_s$ suggest a large diurnal cycle of subsidence, peaking around midday and damping to zero around midnight, although the NCEP analyses are noisier and have a larger semi-diurnal component. The large amplitude of this cycle is associated with a gravity wave driven by daytime heating on the Andean slopes 1500 km away (Garreaud and Muñoz, 2004). This causes a rapid increase in BL thickness at night ($\partial \hat{p}_i / \partial t > 0$) and decrease in BL thickness during the day ($\partial \hat{p}_i / \partial t < 0$). With either analysis, the diurnal cycle of $\hat{\omega}_e$ is qualitatively in accord with expectation for radiatively driven stratocumulus. The implied entrainment rate is large at night ($\hat{\omega}_e = 5 \times 10^{-4}$ mb s^{-1}, or approximately 5 mm s^{-1}) and drops to zero near local noon when cloud heating due to solar absorption could be expected to be largest and most effective at suppressing in-cloud turbulence. The ECMWF results are more believable, since NCEP analysis actually implies significantly negative midday entrainment, which is physically implausible. Additionally, the ECMWF-implied $\hat{\omega}_e$ is quasi-steady throughout the night, which matches expectations since longwave radiative forcing is essentially

steady and large during this time. The average entrainment rates for the 6 days of study are 3.5 mm s^{-1} and 3.2 mm s^{-1} based on the ECMWF and NCEP analyses, respectively. These values compare well with the climatological value of just over 3 mm s^{-1} value obtained by Wood and Bretherton (2004).

4.2 Analysis of the q_t and s_l Budgets

4.2.1 Six-Day Mean

Each term in the mixed-layer moisture and energy budgets (1) and (2) was estimated at each radiosonde launch time using the data described in section 3. The resulting time series were averaged into 6-day means, which are presented in Tables 1 and 2. All terms are given in energy flux units for consistency. The entrainment rates are inferred from the mass budgets. In both budgets there are balances between dominant terms. Table 1 reveals that surface evaporation is balanced primarily by entrainment drying and secondarily by horizontal dry advection. The s_l budget, on the other hand, indicates that longwave cooling and (to a lesser extent) cold advection balance comparable contributions from entrainment, shortwave warming, and sensible heating. Precipitation does not play a significant role in either budget. Although significant cloud base drizzle was observed on several of the study days, a high cloud base (ranging from 800 to 1100 m) meant that almost all precipitation evaporated before reaching the surface (Bretherton et al., 2004; Comstock et al., 2004). Wood (2004) suggests that the EPIC case is not unusual in this regard and that in general, drizzle tends to largely evaporate before

reaching the surface below stratocumulus clouds with bases higher than 500m.

In each table, an estimate of the sampling uncertainty for the 6-day mean is given as

$$\sigma_{\text{mean}} = \sqrt{\frac{1}{6 \cdot 8}\left[\frac{1}{8}\sum_{k=1}^{8}\sigma_k^2\right]} \tag{18}$$

where σ_k is the standard deviation of the data at the kth time of day. Assuming that error is independent of time of day, this quantity is the standard deviation of the 6-day mean. It is important to realize that this error statistic reflects only sampling variability and does not capture biases due to calibration error or to uncertainties in the analysis methods. Additionally, much of σ_k could be due to real synoptic variability rather than an inability to accurately sample quantities at individual times. In this case σ_{mean} may have little to do with the accuracy of a budget term, instead reflecting its representativeness as a longer-term mean to the extent this can be assessed from only 6 days of data. From this perspective, however, σ_k is only a lower bound, since synoptic variations are autocorrelated over periods of several days. In spite of these caveats, we will interpret σ_{mean} for individual budget terms as a rough guide to the representativeness of the balances in our 6-day mean. Taken in this context, the tendencies of both q_t and s_l in the 6-day mean are not significantly different than zero, which is encouraging since having the budget quantities remain constant in time suggests that the averages captured here are representative of a longer-term mean rather than of only our particular 6 days of data. Another indication of useful budgets is that the sampling variability of all remaining budget terms are reassuringly small compared to the magnitude of their mean values.

A second, more robust measure of the uncertainty inherent in the budget calculations is available in the form of 6-day mean budget residuals. It is in assessing these residuals that our error analysis is most compelling, because this error really does reflect sampling inadequacy or biases. These residuals are presented in the last columns of Tables 1 and 2. That the budgets generally don't close to within the calculated uncertainties illustrates that standard error analysis tends to under predict the actual error in this type of study.

Residuals in the NCEP-based budgets are larger than those using ECMWF data. In the q_t budget, this reflects the markedly stronger dry advection in the NCEP model. In the s_l budget, a larger residual results from small differences in NCEP's horizontal advection and subsidence rate. In light of the larger NCEP closure errors, we will restrict our attention to the ECMWF results for the remainder of the paper.

We saw in Fig. 5 that estimation of the time-series of subsidence at a remote ocean location from analyses may be subject to large systematic errors which may depend on the diurnal cycle. These errors may affect the mass-budget estimate of entrainment. Hence, another perspective on the heat and moisture budgets is as a way to get independent estimates of $\hat{\omega}_e$ by solving for the entrainment fluxes as budget residuals in (1) and (2). Applied in this way, the q_t budget yields a 6-day mean entrainment rate of 4.3 mm s^{-1} , while the s_l budget yields 4.7 mm s^{-1} . Comparison of the three independent entrainment estimates for this period suggests a mean entrainment rate for the buoy period of roughly 4 ± 1 mm s^{-1}.

4.2.2 Diurnal Cycle

Only a few terms in the q_t and s_l budgets have diurnal cycles of significant amplitude. These terms are plotted in Fig. 6 (with entrainment fluxes based on $\hat{\omega}_e$ from the ECMWF mass budget). In the moisture budget, decreased entrainment drying during the day results in a buildup of BL moisture, which is then depleted by more vigorous entrainment at night. The diurnal cycle of liquid static energy involves an increase in $\langle s_l \rangle$ during the day due to solar heating, followed by a decrease after sunset which is partially mitigated by enhanced entrainment of warm air from the free troposphere at night.

An estimate of the sampling variability involved in these calculations is made following (18). Day-to-day variability in storage ($= \hat{p}_i \partial / \partial t$ - the rate at which a quantity accumulates in the BL) and entrainment warming/drying are assumed to be independent of time of day, so the error in these quantities should be $\sigma_{di} = \sqrt{8}\sigma_{mean}$ since there are eight times fewer samples for each time of day than for the mean. Shortwave heating - important in the s_l budget - has zero variability at night, rendering (18) inappropriate. Instead, the error bars given on $\nabla F_{SW,\mathrm{net}}$ during the daytime are taken as the standard deviation of the data at that time of day. The sign convention in figure 6 was chosen so that a positive perturbation increases s_l or q_t.

By deriving entrainment fluxes for each time of day as residuals of (1) and (2), we are able to infer time series of entrainment, which are shown in Fig. 7 with error bounds again calculated as $\sqrt{8}\sigma_{\mathrm{mean}}$. The estimates are broadly consistent with the subsidence-based entrainment prediction, with a nocturnal maximum of approximately 5 mm s^{-1}

and a sharp drop toward midday. Both estimates predict the $\hat{\omega}_e$ minimum to occur later than suggested by the subsidence budget. Again, the error bounds provide only a rough measure of sample variability, although evidence of systematic bias is present as well. For example, the q_t budget suggests negative entrainment around midday, which is clearly unphysical. Additionally, confidence bounds in Fig. 7 are disjoint for some methods at some times of day. Comparing Fig. 7 to Fig. 6, we see that the diurnal cycle of entrainment from the q_t and s_l budgets is largely modulated by the diurnal cycle of storage, which is one of the more uncertain measurements in the budgets because it is based on a single radiosonde profile every three hours. Nonetheless, all 3 budgets yield a similar diurnal profile and mean value of w_e, which increases our confidence in the entrainment estimates from the individual budgets.

4.3 Diurnal Cycle of Turbulence

Profiles of buoyancy flux were calculated for each three-hour interval as described in section 2.2, based on ECMWF mass-budget-derived entrainment rates, inferring the turbulent fluxes of q_t and s_l from mixed-layer theory and the buoyancy flux from (12) and (14), assuming the mean cloud base over the three-hour period. Because calculation of the turbulent fluxes depends strongly on the mixed-layer assumption, we emphasize that when the BL is not well-mixed this method of inferring buoyancy flux becomes inappropriate. Fig. 8 shows the 6-day mean diurnal cycle of mixed-layer inferred buoyancy flux. At all times of day, the profiles have the structure expected of a radiatively-driven

cloud-topped mixed layer - small values near the surface decreasing to a minimum at cloud base, then jumping up to reach a maximum value in the cloud. Also apparent is a diurnal cycle in the intensity of buoyancy flux within the cloud. The night-time maximum is the result of strong longwave cooling at cloud top and the daytime minimum is the result of this cooling being canceled by shortwave heating. A related feature is the diurnal variation in the sub-cloud buoyancy flux minimum. Fig. 8a shows substantial negative $\mathcal{B}$ building up below the cloud before sunrise and persisting throughout the day. The existence of negative buoyancy fluxes during the day is an expected consequence of shortwave heating in the cloud. However, sub-cloud buoyancy flux becomes negative before dawn, and reaches a minimum before 8 am, earlier than expected for a BL dominated by shortwave heating. Fig. 8b suggests that the process responsible for these features is the evaporation of drizzle. In this figure, the buoyancy flux has been recalculated with precipitation set to zero. This results in the time of minimum buoyancy flux shifting to around noon and in the disappearance of negative $\mathcal{B}$.

Because significant negative $\mathcal{B}$ leads to BL decoupling (Bretherton and Wyant, 1997; Stevens, 2000), this finding suggests that drizzle may be contributing to partial early-morning BL decoupling. This hypothesis may be investigated by examining the ability of the lifting condensation level (LCL) derived from shipboard measurements to predict cloud base over the course of a day. In a well-mixed BL, surface and cloud base humidity are homogenized by mixing, so the surface LCL will be a good predictor of the actual cloud base. In practice a correction must be applied to the surface LCL to account

for the moisture and temperature gradients within the surface layer. By comparing the average surface LCL to that computed from the sondes at 100m above the surface, we calculate the surface layer to cause an approximately -150m bias to the surface LCL. This is consistent with the correction one would make using the observed air-sea moisture differences and assuming a log-layer between the 15m measurement height and 100m. Fig. 9 compares the 6-day mean diurnal cycle of corrected surface LCL and the ceilometer-measured cloud base. This figure shows that the BL is more well-mixed during the night (though even then there is a slight residual moisture stratification), but rapidly becomes less so in the early morning and remains less well mixed throughout the daylight hours. This phasing corresponds closely to the onset of negative buoyancy flux presented in Fig. 8, corroborating the role of early-morning drizzle and later solar absorption in inhibiting efficient vertical mixing of the BL. Even during these less well-mixed periods, the BL soundings do not exhibit pronounced decoupling such as a distinct scud-capped surface moist layer, which implies some turbulent mixing is apparently continuing. Hence use of the mixed-layer assumption to derive the buoyancy fluxes remains tenable throughout the day.

4.4 Entrainment Parameterization

Conceptually, entrainment results when large eddies penetrate the inversion capping the BL, lose momentum, and fall back through the inversion, drawing filaments of free-tropospheric air back down with them (Turner, 1973). As such, many entrainment

parameterizations have tended to focus on quantifying the strength of these eddies and the efficiency with which they entrain the overlying air. In a cloud-free convectively driven BL the relation

$$\frac{w_e}{w_*} = A \cdot Ri^{-1} \tag{19}$$

was found to hold well with w_* as defined in (15), bulk Richardson number $Ri = \frac{\Delta b \cdot z_i}{w_*^2}$ (where the inversion density jump Δb is expressed in buoyancy units) and empirically-derived entrainment efficiency rate $A \approx 0.2$ (Driedonks, 1982; Deardorff, 1983). In the presence of cloud, however, (19) ceases to fit the data as written. In this regime, values of A between 1 and 5 have been inferred from aircraft observations (mostly during daytime), with considerable spread between experiments (Nicholls and Turton, 1986; de Roode and Duynkerke, 1997; Faloona et al., 2004). Such inferences are complicated by the possibility of decoupling, which could result in the appropriate vertical eddy scale being smaller than z_i, which would cause an over prediction of A. The composite diurnal cycle of w_e and w_* inferred from the EPIC data is consistent with these results. Fig. 10 shows the relation between w_e and $w_* Ri^{-1}$ for both the 8 samples of the EPIC diurnal cycle and for the DYCOMS II data, almost all of which is nocturnal. Both data sets support a similar dependence of entrainment on $w_* Ri^{-1}$, with the EPIC data lying along a best fit line (drawn in dashes) with slope corresponding to an A value of 1.2. It should be noted that considerable uncertainty exists in this calculation. For example, the bar corresponding to 11am local time does not fall on the best-fit line because the entrainment inferred for this time is negative - an unphysical prediction. Additionally,

entrainment from the mass budget is used both as the independent variable and in the w_* calculation, which could bias the results. Further, the mixed-layer assumption is employed here for all times of day in calculating w_*, even though Fig. 9 suggests that the well-mixed assumption is not perfectly satisfied throughout daylight hours.

Measurement uncertainty alone, however, is unlikely to account for the wide spread in A reported in the literature. There is no reason A should be a universal constant in cloud-topped mixed layers. Clouds affect turbulence (and thus, perhaps, entrainment) in a multitude of ways which could depend on environmental conditions in a manner not captured by (19) with A held constant. Choosing which of these processes are important and finding a way to include these processes in a parameterization is at the heart of the current entrainment debate.

We now compare our observations with the predictions of a few recent parameterizations, each of which emphasizes a different cloud process for diagnosing entrainment. The first of these schemes was proposed by Turton and Nicholls (1987). This scheme, hereafter denoted NT, accounts for the enhancement of turbulence by evaporative cooling at cloud top by replacing Δb in (19) with

$$\Delta b_{NT} = \frac{\Delta b}{1 + a_2 \cdot \left(1 - \frac{\Delta m}{\Delta b}\right)}$$

where $\Delta m = 2 \int_0^1 \Delta b\,(\chi)\, d\chi$. Here, $\Delta b\,(\chi)$ is the cloud-top buoyancy jump (including evaporative cooling) caused by mixing χ parts inversion air with $1 - \chi$ parts cloudy air so that Δm is proportional to the average evaporative enhancement over all possible mixtures. Turton and Nicholls found a_2=60 to fit their data well, although a recent

regional model simulation of subtropical stratocumulus suggests that a_2=15 provides better results when this scheme is implemented within a BL-turbulence parameterization. (McCaa and Bretherton, 2004). Entrainment predictions using both values are considered here.

The second parameterization comes from Lilly (2002a). This proposal (hereafter DL) also accounts for cloud-top evaporation, this time by replacing Δb in (19) with $\Delta b_{DL} = \alpha \Delta_{\text{sat}} b + (1-\alpha)\Delta_{\text{dry}} b$. This correction was designed to fit Lilly's observation that cloud-top dynamics seem to be a combination of the values predicted independently for saturated and dry microphysics. The optimal combination of the two cases was chosen empirically to be $\alpha = \tanh(2.45 \cdot m_*)/\tanh(2.45)$ where m_* is the mixing fraction sufficient to just evaporate the cloud. The other interesting feature of the DL scheme is that turbulence generated at cloud top is weighted more heavily than that generated at the surface by replacing w_* in (19) with $w_{*,DL} = \left[3 \int_0^{z_i} \frac{z}{z_i} \mathcal{B} dz\right]^{1/3}$.

Finally, we consider the parameterization in Lewellen and Lewellen (1998) (hereafter LL), which is based on a rather different hypothesis - that entrainment is controlled by large-eddy energetics. LL assume that a fixed fraction of the TKE generated in the absence of entrainment is depleted through entrainment mixing of buoyant air from the inversion down into the BL. Assuming once again that buoyancy flux is the main source of TKE, the LL parameterization may be written

$$\eta = \int_0^{z_i} \left[\mathcal{B}_{NE} - \mathcal{B}\right] dz / \int_0^{z_i} \mathcal{B}_{NE} dz$$

where η is taken as .35 on the basis of large-eddy simulations and $\mathcal{B}_{NE}$ is the buoyancy

flux in the absence of entrainment. They also includes a correction for radiative cooling in the inversion layer which we omit on the basis that it is not clear how this value should be calculated from the EPIC data, or whether it is even physically relevant (Lilly, 2002b). Other parameterizations could be tested against our data; we selected these three because the comparison is straightforward yet the parameterizations are still fairly different.

A comparison of these parameterizations is presented in Fig. 11. Except for the NT parameterization with a_2=60, all of the schemes agree closely with each other and quite well with the EPIC data. The agreement between the three parameterizations is remarkable, especially since the LL closure completely neglects evaporative enhancement, which plays an essential role in the other two closures. These schemes performed similarly well in a comparison with entrainment observations from the first research flight of DYCOMS II (Stevens et al., 2003). Successful simulation of the entrainment rates from EPIC is impressive because it implies that the closures exhibit the proper sensitivity to the diurnal cycle. Like most other studies, however, our comparison involves large uncertainties. Longer-term measurements similar to those made in EPIC would be extremely useful for reducing these errors.

5 Conclusions

A clean diurnal cycle sampled by an extensive set of shipborne measurements during EPIC 2001 has provided an excellent opportunity to study the diurnally-varying mass, heat, and water budgets of the SE Pacific stratocumulus region and their implications

for entrainment and decoupling. We have combined frequent radiosonde observations, ship-based remote sensing of cloud properties, a radiative-transfer model, and surface turbulent flux measurements with ECMWF and NCEP analyses of subsidence and horizontal advection to evaluate all terms in these budgets during a 6-day period. The mean budgets over this period showed balances expected for stratocumulus. The diurnal variation of entrainment and the associated warming and drying were balanced by diurnal variations in storage and in the absorption of insolation. Each budget provided an independent estimate of the diurnal cycle of entrainment rate as a budget residual. All three estimates have similar daily means and a consistent diurnal cycle. This cycle consists of fairly constant entrainment rates of 5 mm s^{-1} throughout the night, dropping to near zero by midday before recovering in the evening for a daily mean value of 4 mm $^{-1}$.

Buoyancy flux profiles inferred from this analysis show that drizzle, which is negligible in terms of its direct effect on the water and energy budgets (because it largely evaporates before reaching the surface), nonetheless exerts a strong influence on BL dynamics by limiting turbulent mixing below cloud base and thereby promoting decoupling. Independent evidence of partial decoupling is found in the form of increased LCL/cloud base difference during early morning to late afternoon, although even then residual mixing keeps BL internal gradients of conserved variables relatively small so a mixed layer approximation is still reasonable. The buoyancy flux profiles are used to test selected entrainment closures, which performed surprisingly well in predicting the

correct diurnal cycle of entrainment. That such an internally consistent picture of entrainment into a stratocumulus-capped mixed layer could be obtained from ship-based observations alone is quite remarkable, and is a testament to the suite of ship-based measurements made during EPIC. Coordination of a similar set of measurements with an airborne field campaign could better test this approach and further advance our understanding of the interplay between entrainment, turbulence, drizzle, and the diurnal cycle in stratocumulus.

Acknowledgments

The authors which to thank Martin Köhler for use of the ECMWF analyses and Hua-Lu Pan and Steve Krueger for the NCEP data. We are also grateful to Christopher Fairall, Taneil Uttal and Duane Hazen of NOAA ETL for providing MMCR data and information, and to the crew of the NOAA RHB for their assistance during the EPIC cruise. This research was funded by NSF grant ATM0082384 and NASA grant NAGS-10624.

Appendix: Derivation of Budget Equations

If $A = q_t$ or s_l, the time tendency of A can be written in terms of the convergence of its flux F_A,

$$\frac{\partial A}{\partial t} + \mathbf{v} \cdot \nabla_h A + w \frac{\partial A}{\partial z} = -\frac{1}{\rho} \nabla \cdot F_A \tag{1}$$

where ∇_h is the horizontal divergence operator (the vertical divergence is considered explicitly). The large-scale pressure field is in hydrostatic balance and by classical Boussinesq scaling assumptions, horizontal pressure perturbations are negligibly small compared to those in the vertical, so at any $\hat{p}$, $\partial\hat{p} = \rho g \partial z$ and by extension $\hat{\omega} = \rho g w$. Applying this relation to (1),

$$\frac{\partial A}{\partial t} + \mathbf{v} \cdot \nabla_h A + \hat{\omega}\frac{\partial A}{\partial \hat{p}} = -\frac{1}{\rho}\nabla_h \cdot F_A - g\frac{\partial F_A}{\partial \hat{p}}. \tag{2}$$

Reynolds averaging this last equation and noting that conservation of mass implies $\partial u/\partial x + \partial v/\partial y + \partial\hat{\omega}/\partial\hat{p} = 0$,

$$\frac{\partial \overline{A}}{\partial t} + \overline{\mathbf{v}} \cdot \nabla_h \overline{A} + \hat{\omega}_s\frac{\partial \overline{A}}{\partial \hat{p}} + \frac{\partial \overline{\hat{\omega}' A'}}{\partial \hat{p}} = -g\frac{\partial \overline{F_A}}{\partial \hat{p}} \tag{3}$$

where overbars denote horizontally-averaged quantities, primes imply perturbations from this average, and it is recognized that $\overline{\hat{\omega}}$ is the subsidence rate, $\hat{\omega}_s$. In this equation, $\nabla_h \cdot \overline{\hat{\omega}' A'}$ and $\nabla_h \cdot \overline{F_A}$ have been neglected in recognition of their relative insignificance when compared to the vertical gradients. Integrating over the BL depth $\hat{p}_i$, (3) becomes

$$\int_0^{\hat{p}_i} \frac{\partial \overline{A}}{\partial t} d\hat{p} + \hat{p}_i \left\langle \overline{\mathbf{v}} \cdot \nabla_h \overline{A} \right\rangle + \int_0^{\hat{p}_i} \hat{\omega}_s \frac{\partial \overline{A}}{\partial \hat{p}} d\hat{p} + \overline{\hat{\omega}' A'}|_0^{\hat{p}_i} = -g F_A|_0^{\hat{p}_i} \tag{4}$$

where angle brackets refer to BL-averaged quantities. The first term in (4) can be simplified by noting that

$$\begin{aligned}
\int_0^{\hat{p}_i} \frac{\partial \overline{A}}{\partial t} d\hat{p} &= \frac{\partial}{\partial t}\int_0^{\hat{p}_i} \overline{A} d\hat{p} - \frac{\partial \hat{p}_i}{\partial t}\overline{A}|_{\hat{p}_i -} && (5)\\
&= \frac{\partial \left(\hat{p}_i \left\langle \overline{A} \right\rangle\right)}{\partial t} - \frac{\partial \hat{p}_i}{\partial t}\overline{A}|_{\hat{p}_i -} && (6)\\
&= \left[\left\langle \overline{A} \right\rangle - \overline{A}|_{\hat{p}_i}\right]\frac{\partial \hat{p}_i}{\partial t} + \hat{p}_i \frac{\partial \overline{A}}{\partial t}. && (7)
\end{aligned}$$

The third term in (4) may be rewritten as

$$\int_0^{\hat{p}_i} \hat{\omega}_s \frac{\partial \overline{A}}{\partial \hat{p}} d\hat{p} = \int_0^{\hat{p}_i} \frac{\partial \left(\hat{\omega}_s \cdot \overline{A}\right)}{\partial \hat{p}} d\hat{p} - \int_0^{\hat{p}_i} \overline{A} \frac{\partial \hat{\omega}_s}{\partial \hat{p}} d\hat{p} \tag{8}$$

$$= \hat{\omega}_s \cdot \overline{A}|_{\hat{p}_{i-}} - \frac{\partial \hat{\omega}_s}{\partial \hat{p}} \cdot \hat{p}_i \left\langle \overline{A} \right\rangle \tag{9}$$

$$= \hat{\omega}_s \left[\overline{A}|_{\hat{p}_i} - \left\langle \overline{A} \right\rangle \right]. \tag{10}$$

In the above equation, the second equality follows from assuming that horizontal divergence, $-\partial\hat{\omega}_s/\partial\hat{p}$, is constant in height (a reasonable assumption in the lowest 2-3 km of the subtropical troposphere) and noting that $\hat{\omega}_s = 0$ at the surface. The final line results from noting that if $\partial\hat{\omega}_s/\partial\hat{p}$ is height independent, $\hat{p}_i \, \partial\hat{\omega}_s/\partial\hat{p} = \hat{\omega}_s|_{\hat{p}_i}$.

Applying (7) and (10) to (4) and noting that BL-integrated mass continuity implies $\overline{\hat{\omega}'A'}|_{\hat{p}_i} = -\hat{\omega}_e \left(\overline{A}|_{\hat{p}_{i+}} - \overline{A}|_{\hat{p}_{i-}} \right)$,

$$\hat{p}_i \left[\frac{\partial \overline{A}}{\partial t} + \left\langle \overline{\mathbf{v}} \cdot \nabla_h \overline{A} \right\rangle \right] + \left(\hat{\omega}_s - \frac{\partial \hat{p}_i}{\partial t} + \hat{\omega}_e \right) \left[\overline{A}|_{\hat{p}_{i-}} - \left\langle \overline{A} \right\rangle \right] - \hat{\omega}_e \left[\overline{A}|_{\hat{p}_{i+}} - \langle A \rangle \right] - \overline{\hat{\omega}'A'}|_0 + gF_A|_0^{\hat{p}_i} = 0. \tag{11}$$

Defining $\Delta A = \left[\overline{A}|_{\hat{p}_{i+}} - \langle A \rangle \right]$ and noting that $\hat{\omega}_s - \frac{\partial \hat{p}_i}{\partial t} + \hat{\omega}_e = \overline{\mathbf{v}} \cdot \nabla_h \hat{p}_i$,

$$\hat{p}_i \left[\frac{\partial \overline{A}}{\partial t} + \left\langle \overline{\mathbf{v}} \cdot \nabla_h \overline{A} \right\rangle \right] - \overline{\hat{\omega}'A'}|_0 + gF_A|_0^{\hat{p}_i} - \hat{\omega}_e \Delta A = \left[\langle A \rangle - \overline{A}|_{\hat{p}_{i-}} \right] \overline{\mathbf{v}} \cdot \nabla_h \hat{p}_i \tag{12}$$

which yields the budget equations presented in this study when $\overline{A}$ is replaced by q_t (which makes the turbulent surface flux $g \cdot \frac{\text{LHF}}{L}$ and the flux function $F_{q_t} = F_P$) or by s_l (in which case $\overline{\hat{\omega}'A'}|_0 = g \cdot$SHF and $F_{s_l} = L \cdot F_P + F_R$).

References

Albrecht, B., C. Fairall, D. Thomson, et al.: 1990, Surface-based remote-sensing of the observed and the adiabatic liquid water-content of stratocumulus clouds. *Geophys. Res. Lett.*, **1**, 89–92.

Bretherton, C. S., T. Uttal, C. W. Fairall, S. E. Yuter, R. A. Weller, D. Baumgardner, K. Comstock, and R. Wood: 2004, The EPIC 2001 stratocumulus study. *BAMS*, **85**, 967–977.

Bretherton, C. S. and M. C. Wyant: 1997, Moisture transport, lower-tropospheric stability, and decoupling of cloud-topped boundary layers. *J. Atmos. Sci.*, **54**, 148–167.

Brost, R. A., J. C. Wyngaard, and D. H. Lenschow: 1982, Marine stratocumulus layers. part II: Turbulence budgets. *J. Atmos. Sci.*, **39**, 818–836.

Caughey, S., B. Crease, and W. Roach: 1982, A field study of nocturnal stratocumulus II: Turbulence structure and entrainment. *Quart. J. R. Met. Soc.*, **108**, 125–144.

Comstock, K., R. Wood, S. E. Yuter, and C. S. Bretherton: 2004, Reflectivity and rain rate in and below drizzling stratocumulus, in press.

de Roode, S. R. and P. G. Duynkerke: 1997, Observed lagrangian transition of stratocumulus into cumulus during ASTEX: mean state and turbulence structure. *J. Atmos. Sci.*, **54**, 2157–2173.

Deardorff, J.: 1983, A multi-limit mixed-layer entrainment formulation. *J. Phys. Oceanogr.*, **13**, 988–1002.

Dong, X. and G. G. Mace: 2003, Arctic stratus cloud properties and radiative forcing derived from ground-based data collected at Barrow, Alaska. *J. Climate*, **16**, 445–460.

Driedonks, A.: 1982, Models and observations of the growth of the atmospheric boundary layer. *Boundary-Layer Meteorol.*, **23**, 283–306.

Duynkerke, P. G. and J. Teixeira: 2001, Comparison of the ECMWF reanalysis with FIRE I observations: Diurnal variation of marine stratocumulus. *J. Clim.*, **14**, 1466–1478.

Fairall, C. W., E. F. Bradley, D. P., Rogers, J. B. Edson, and G. S. Young: 1996, Bulk parameterization of air-sea fluxes for tropical ocean global atmosphere coupled ocean atmospere response experiment. *Journal of Geophysical Research - Oceans*, **101**, 3747–3764.

Faloona, I., D. Lenschow, T. Campos, B. Stevens, M. van Zanten, B. Blomquist, D. Thornton, A. Bandy, and H. Gerber: 2004, Observations of entrainment in Eastern Pacific marine stratocumulus using three conserved scalars, accepted.

Garreaud, R. D. and R. Muñoz: 2004, The diurnal cycle in circulation and cloudiness over the tropical southeast Pacific: A modeling study. *J. Climate*, 1669–1710.

Hartmann, D., M. Ockert-Bell, and M. Michelson: 1992, The effect of cloud type on Earth's energy balance: Global analysis. *J. Climate*, 1281–1304.

Hignett, P.: 1991, Observations of diurnal-variation in a cloud-capped marine boundary-layer. *J. Atmos. Sci.*, **12**, 1474–1482.

Hogg, D. C., F. O. Guiraud, J. B. Snider, M. T. Deckerand, and E. R. Westwater: 1983, A steerable dual-channel microwave radiometer for the measurement of water vapor and liquid in the troposphere. *J. Clim./Appl. Meteorol.*, **5**, 789–806.

Klein, S. A. and D. L. Hartmann: 1993, The seasonal cycle of low stratiform clouds. *J. Climate*, **6**, 1587–1606.

Lenschow, D. H., M. Y. Zhou, L. S. Chen, and X. D. Xu: 2000, Measurements of fine-scale structure at the top of marine stratocumulus. *Boundary Layer Meteorology*, **97**, 331–357.

Lewellen, D. and W. Lewellen: 1998, Large-eddy boundary layer entrainment. *J. Atmos. Sci.*, **55**, 2645–2665.

Lilly, D.: 1968, Models of cloud-topped mixed layers under a strong inversion. *Quart. J. Roy. Meteor. Soc.*, 292–303.

— 2002a, Entrainment into mixed layers. part I: Sharp-edged and smoothed tops. *J. Atmos. Sci.*, **59**, 3340–3352.

— 2002b, Entrainment into mixed layers. part II: A new closure. *J. Atmos. Sci.*, 3353–3361.

McCaa, J. and C. Bretherton: 2004, A new parameterization for shallow cumulus convection and its application to marine subtropical cloud-topped boundary layers. part II: Regional simulations of marine boundary layer clouds. *Mon. Wea. Rev.*, **132**, 883–896.

McClatchey, R., R. Fenn, J. Selby, F. Volz, and J. Garing: 1971, Optical properties of the atmosphere. Technical Report Rep. AFCRL-71-0279, Air Force Cambridge Res. Lab., Hanscom AFB, Bedford MA.

Nicholls, S.: 1984, The dynamics of stratocumulus: aircraft observations and comparisons with a mixed layer model. *Quart. J. Roy. Meteor. Soc.*, **110**, 783–820.

Nicholls, S. and J. Leighton: 1986, An observational study of the structure of stratiform cloud sheets: Part I. structure. *Quart. J. Roy. Meteorol. Soc.*, **112**, 431–460.

Nicholls, S. and J. Turton: 1986, An observational study of the structure of stratiform cloud sheets: Part II. entrainment. *Quart. J. Roy. Meteorol. Soc.*, **112**, 461–480.

Randall, D.: 1980, Conditional instability of the first kind upside-down. *J. Atmos. Sci.*, **37**, 125–130.

Randall, D., S. Krueger, C. Bretherton, et al.: 2003, Confronting models with data - the GEWEX cloud systems study. *Bull. Amer. Meteor. Soc.*, **4**, 455–469.

Rozendaal, M., C. B. Leovy, and S. A. Klein: 1995, An observational study of diurnal variations of marine stratiform cloud. *J. Climate*, 1795–1809.

Schubert, W. H., J. S. Wakefield, E. J. Steiner, and S. K. Cox: 1979, Marine Stratocumulus Convection. Part I: Governing Equations and Horizontally Homogenous Solutions. *J. Atmos. Sci.*, **36**, 1286–1307.

Stephens, G., P. Partain, and P. Gabriel: 2001, Parameterization of atmospheric radiative transfer. part I: Validity of simple models. *J. Atmos. Sci.*, **48**, 3391–3409.

Stevens, B.: 2000, Cloud transitions and decoupling in shear-free stratocumulus-topped boundary layers. *Geophys. Res. Lett.*, **27**, 2557–2560.

— 2002, Entrainment in stratocumulus-topped mixed layers. *Quart. J. Roy. Meteorol. Soc.*, **128**, 2663–2689.

Stevens, B., D. H. Lenschow, I. Faloona, C.-H. Moeng, D. K. Lilly, B. Blomquist, G. Vali, A. Bandy, T. Campos, H. Gerber, S. Haimov, B. Morley, and D. Thornton: 2003, On entrainment rates in nocturnal marine stratocumulus. *Quart. J. Roy. Meteor. Soc.*, **84**, 3469–3493.

Turner, J.: 1973, *Buoyancy Effects in Fluids*. Cambridge Press, 360pp.

Turton, J. and S. Nicholls: 1987, A study of the diurnal variation of stratocumulus using a multiple mixed layer model. *Q.J.R. Meteorol. Soc*, **113**, 969–1009.

Weare, B.: 1996, Evaluation of the vertical structure of zonally averaged cloudiness and its variability in the atmospheric model intercomparison project. *J. Climate*, 3419–3431.

Wood, R.: 2004, Drizzle in stratocumulus clouds. Part I: Aircraft observations, in revision - J. Atmos. Sci.

Wood, R. and C. S. Bretherton: 2004, Boundary layer depth, entrainment, and decoupling in the cloud-capped subtropical and tropical marine boundary layer. *Journal of Climate*, **17**, 3576–3588.

Wood, R., C. S. Bretherton, and D. L. Hartmann: 2002, Diurnal cycle of liquid water path over the subtropical and tropical oceans. *Geophys. Res. Lett.*, **29**.

Wood, R. and J. P. Taylor: 2001, Liquid water path variability in unbroken marine stratocumulus. *Quart. J. Roy. Meteorol. Soc.*, **127**, 2635–2662.

	$-\frac{L\hat{p}_i}{g}\frac{\partial\langle q_t\rangle}{\partial t}$	$-\frac{L\hat{p}_i}{g}\langle \mathbf{u}\cdot\nabla_h q_t\rangle$	LHF	$-LF_p(0)$	$\frac{L}{g}\omega_e\Delta q_t$	Residual
		ECMWF/NCEP			ECMWF/NCEP	ECMWF/NCEP
Mean:	-5	-26/-50	99	-5	-68/-61	-5/-22
St. Dev:	9	7/2	2	1	10/8	15/12

Table 1: Forcings to q_t budget, scaled into W m^{-2}.

	$-\frac{\hat{p}_i}{g}\frac{\partial s_l}{\partial t}$	$-\frac{\hat{p}_i}{g}\langle \mathbf{u}\cdot\nabla_h s_l\rangle$	SHF	$-LP(0)$	$-\nabla_{\mathrm{BL}}\cdot F_{SW}$	$-\nabla_{\mathrm{BL}}\cdot F_{LW}$	$\frac{1}{g}\omega_e\Delta s_l$	Residual
		ECMWF/NCEP					ECMWF/NCEP	ECMWF/NCEP
Mean:	0	-19/-20	14	5	26	-78	41/38	11/6
St. Dev:	3	3/1	1	1	1	1	6/5	8/6

Table 2: Forcings to s_l budget, scaled into W m^{-2}.

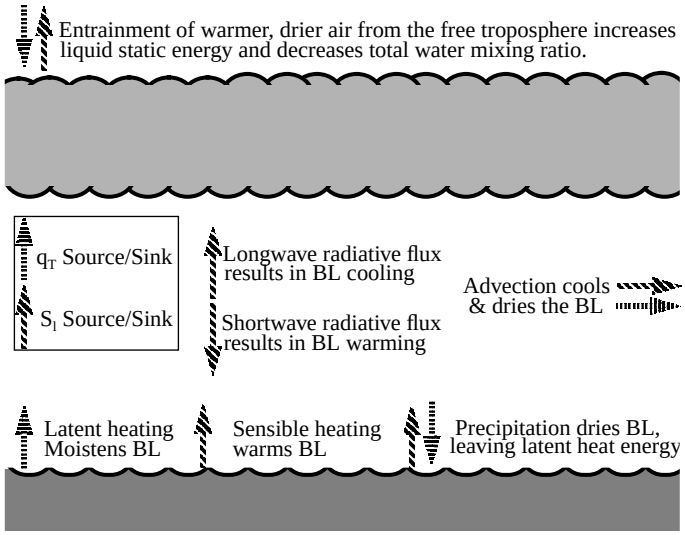

Figure 1: Schematic of BL indicating sources and sinks of $\overline{q_t}$ and $\overline{s_l}$.

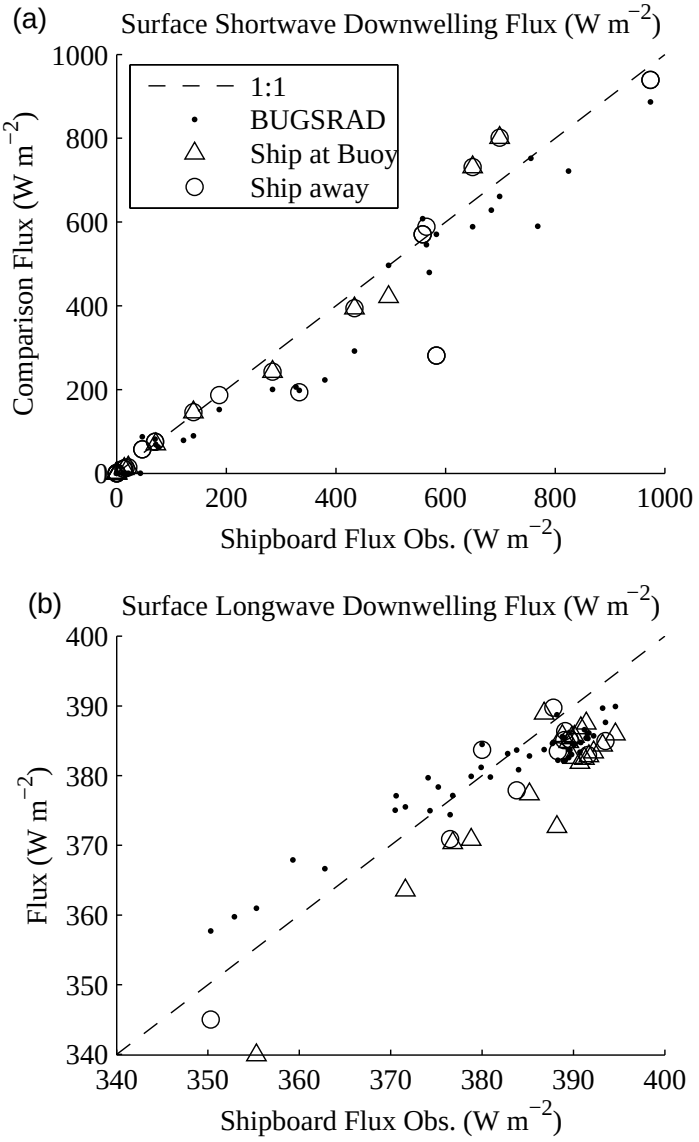

Figure 2: Comparison of observed downwelling flux at the surface with values calculated using the BUGSRAD scheme. Coincident observations from the IMET buoy are included where available. Observations made when the RHB is located at the buoy are indicated by triangles. Values when the RHB is located near but not at the buoy are also included as circles.

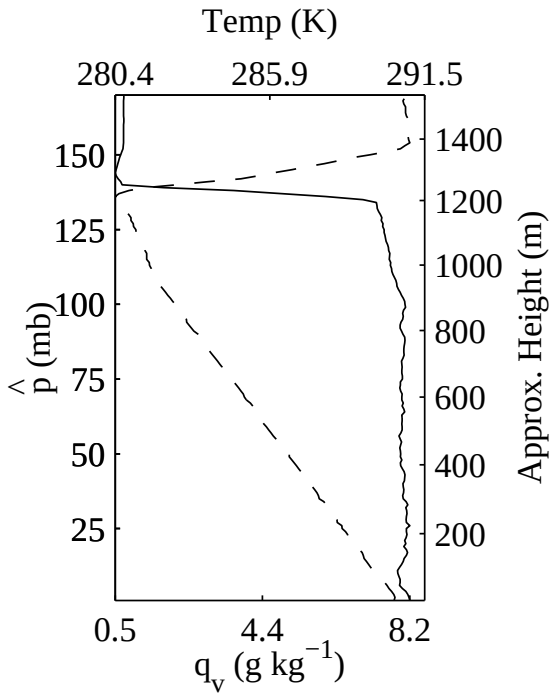

Figure 3: Mixing ratio (solid line) and temperature (dashed line) profiles from the radiosonde launched at 2 UTC (8pm local) on Oct 16, 2001. The temperature inversion appears to be around 15mb (≈150m) deep - twice as thick as the moisture inversion.

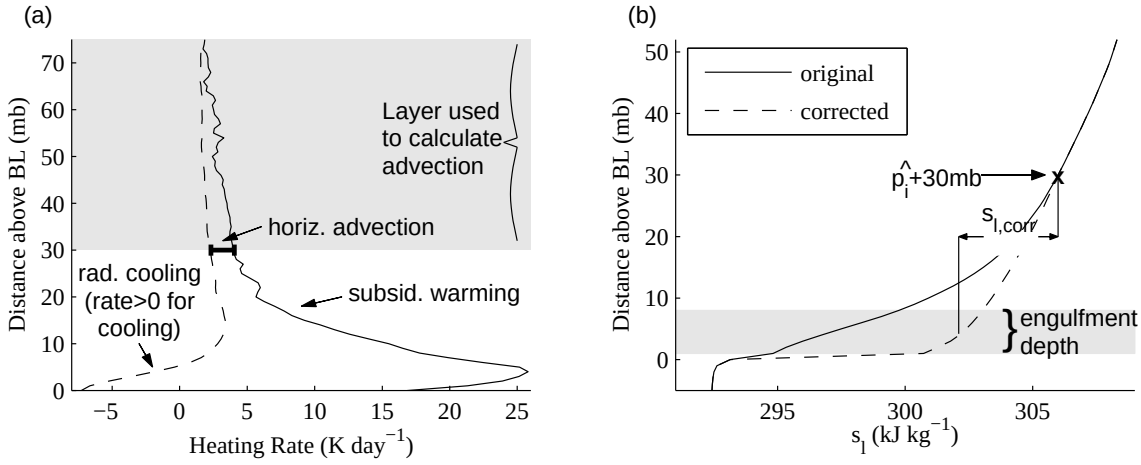

Figure 4: (a) Heating rate due to subsidence warming (solid lines, positive numbers indicate warming) and radiative cooling (dashed lines, positive numbers correspond to cooling). The layer used to calculate advection is indicated in the upper right-hand corner. In this region, the difference between subsidence warming and radiative cooling is interpreted as the advective tendency. A linear fit to this difference is used to diagnose advection in the region between this layer and cloud-top. (b) The uncorrected (solid) and corrected (dashed) s_l profiles along with a diagrammatic description of the correction method.

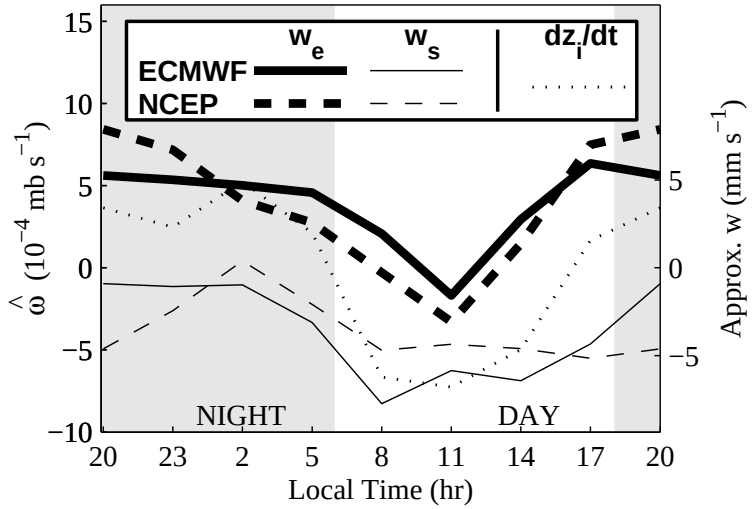

Figure 5: Diurnal cycle of entrainment as diagnosed from the BL mass budget. Entrainment rates are denoted by thick lines, subsidence rates by thin lines, and sonde-derived BL height tendency by dots. ECMWF values are presented in unbroken lines, while NCEP values are dashed.

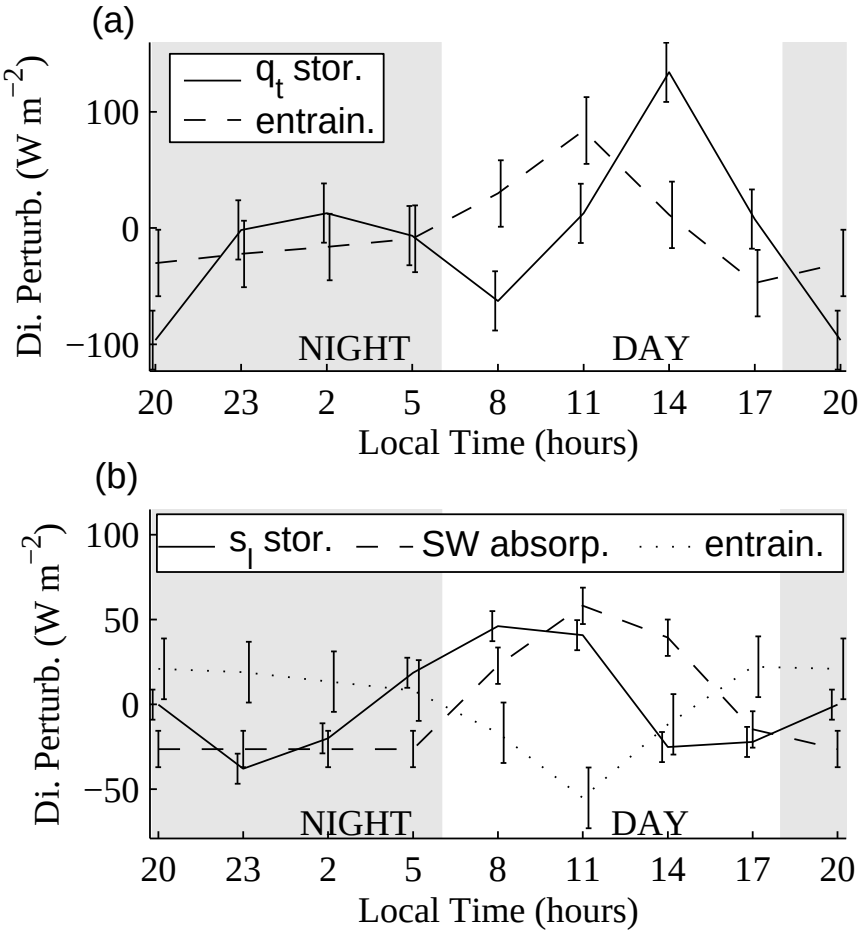

Figure 6: Diurnal cycle for budget terms with diurnal amplitude greater than 20W m^{-2}. For ease of comparison, means have been removed from each term.

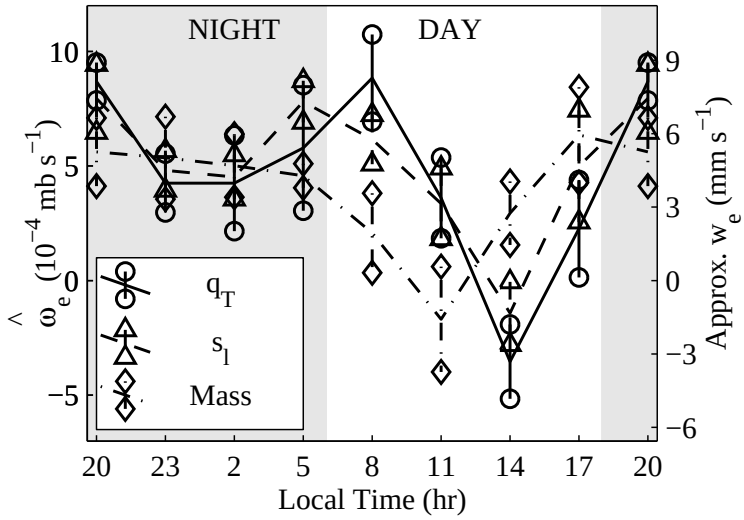

Figure 7: Comparison of the diurnal cycle of entrainment as calculated from the q_t budget (solid lines, circular endpoints on error bars), from the s_l budget (dashed lines, triangular endpoints), and from the subsidence method (dot-dashed lines, diamond endpoints). Error bars represent one standard deviation limits on the mean associated with sample variability over the 6 days.

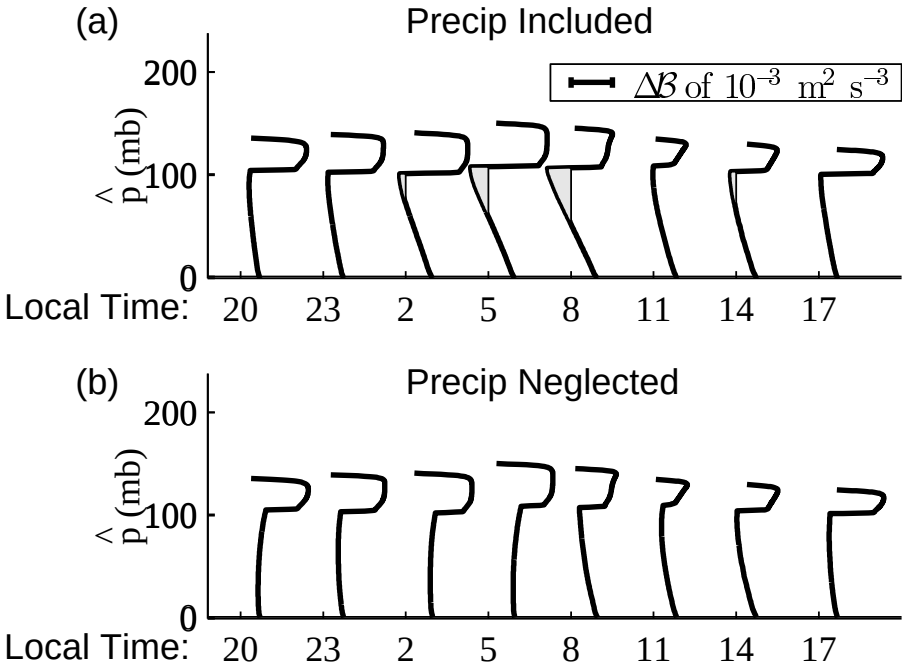

Figure 8: Diurnally-composited buoyancy flux profiles (a) including and (b) excluding the precipitation flux contribution. The tick mark above each time indicates the line of zero-$\mathcal{B}$ for that time; regions of negative buoyancy flux are shaded. A sense of the magnitude of $\mathcal{B}$ may be obtained from the scale in the upper-left corner of (a).

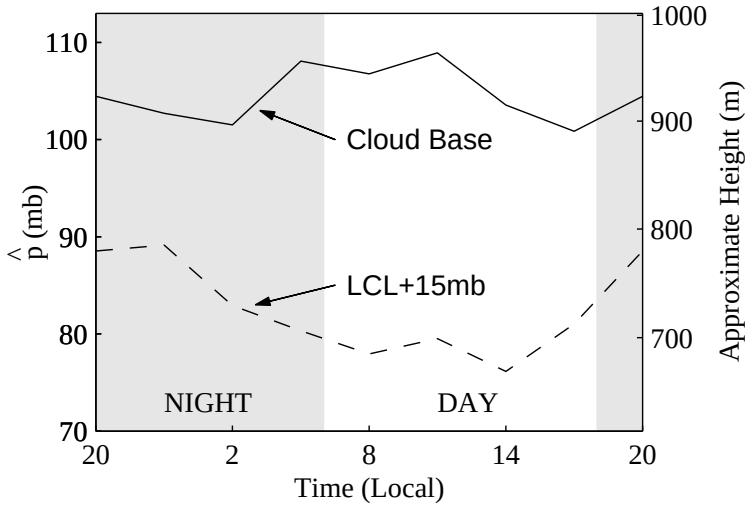

Figure 9: Comparison between diurnal cycle of cloud base and that of LCL. LCL values are shifted up 15mb to account for the effect of the surface layer.

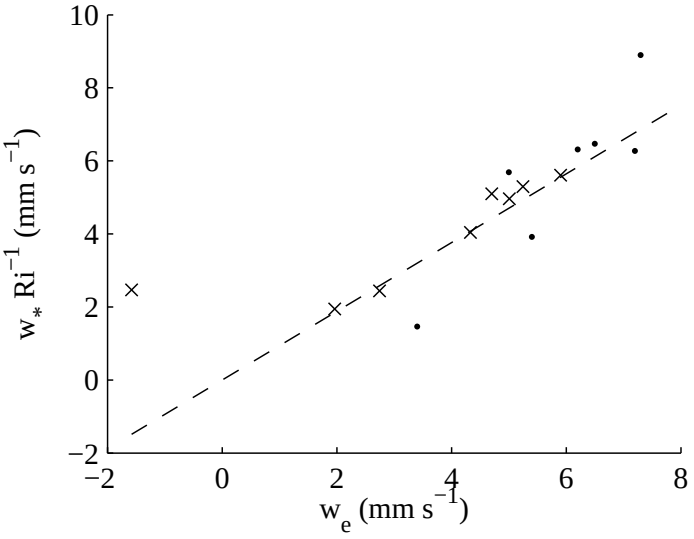

Figure 10: Comparison of entrainment efficiency for the EPIC and DYCOMS II data. DYCOMS II results are presented as dots, while EPIC data is denoted by 'x'. The dashed line is the best fit to the EPIC data (constrained to pass through the origin). The reciprocal of this slope is the best fit estimate of A.

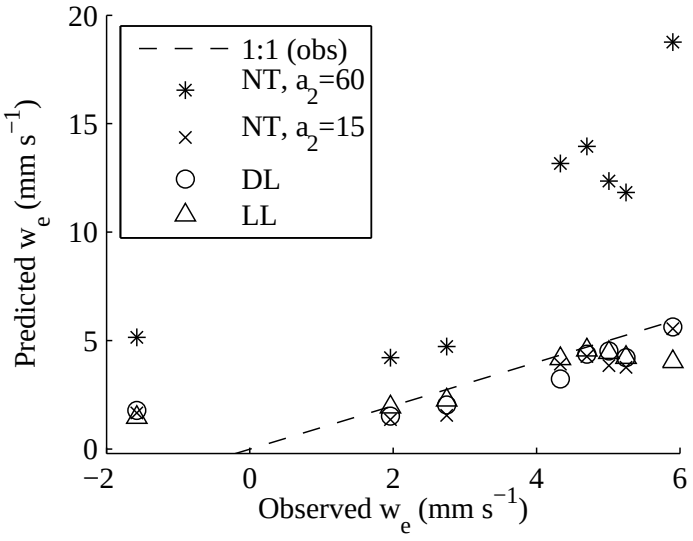

Figure 11: Entrainment rates predicted by the various schemes for each of the eight times of day plotted against the observed entrainment rate. The 1:1 line (dashed) depicts perfect agreement with the observations.